

# **1 Low-temperature non-equilibrium synthesis of anisotropic multimetallic 2 nanosurface alloys for electrochemical CO<sub>2</sub> reduction**

**3 Cedric David Koolen<sup>1,2,3</sup>, Emad Oveisi<sup>4</sup>, Jie Zhang<sup>1,2</sup>, Mo Li<sup>1,2</sup>, Olga V. Safonova<sup>5</sup>, Jack K.  
4 Pedersen<sup>6</sup>, Jan Rossmeisl<sup>6</sup>, Wen Luo<sup>7\*</sup>, Andreas Züttel<sup>1,2</sup>**

**5** <sup>1</sup>Laboratory of Materials for Renewable Energy (LMER), Institute of Chemical Sciences and  
**6** Engineering (ISIC), Basic Science Faculty (SB), École polytechnique fédérale de Lausanne (EPFL)  
**7** Valais/Wallis, Energypolis, Sion, 1951, Switzerland.

**8** <sup>2</sup>Empa Materials Science & Technology, Dübendorf, 8600, Switzerland.

**9** <sup>3</sup>Scidentify SA, 1950, Sion, Switzerland.

**10** <sup>4</sup>Interdisciplinary Centre for Electron Microscopy (CIME), École Polytechnique Fédérale de Lausanne  
**11** (EPFL), CH-1015 Lausanne, Switzerland.

**12** <sup>5</sup>Paul Scherrer Institute, Forschungsstrasse 111, 5232, Villigen, Switzerland

**13** <sup>6</sup>Center for High Entropy Alloy Catalysis (CHEAC), Department of Chemistry, University of  
**14** Copenhagen, 2100 København Ø, Denmark

**15** <sup>7</sup>School of Environmental and Chemical Engineering, Shanghai University, Shanghai, 200444, China.

**16** \*Corresponding author: [wenluo@shu.edu.cn](mailto:wenluo@shu.edu.cn)

**17**

## **18 Abstract**

**19** Multimetallic nanoparticles are of interest as functional materials due to their highly tunable  
**20** properties. However, synthesizing congruent mixtures of immiscible components is limited by  
**21** the need for high-temperature procedures followed by rapid quenching which lack size and  
**22** shape control. Here, we report a low-temperature ( $\leq 80$  °C) non-equilibrium synthesis of  
**23** nanosurface alloys (NSAs) with tunable size, shape and composition regardless of miscibility.  
**24** We show the generality of our method by producing both bulk miscible and immiscible  
**25** monodisperse anisotropic Cu-based NSAs of up to three components. We demonstrate our  
**26** synthesis as a screening platform to investigate the effects of crystal facet and elemental  
**27** composition by testing tetrahedral, cubic and truncated-octahedral NSAs as catalysts in the  
**28** electroreduction of CO<sub>2</sub>. The use of machine-learning has enabled the prediction and informed  
**29** synthesis of both multicarbon-product selective and phase-stable Cu-Ag-Pd compositions. This  
**30** combination of non-equilibrium synthesis and theory-guided candidate selection is expected to  
**31** accelerate test-learn-repeat cycles of structure-performance optimization processes.

## 33 1. Introduction

34 Multimetallic nanoparticles are becoming increasingly important in fields such as  
35 heterogeneous, electro- and photo-catalysis.<sup>[1],[2],[3],[4],[5],[6],[7]</sup> They offer a unique advantage in  
36 tuning the surface electronic and geometric structure, beyond size, support and facet effects.  
37 When coupled with advanced simulations to predict the most active and selective multimetallic  
38 candidate,<sup>[8]</sup> theory-guided catalyst selection can greatly accelerate test-learn-repeat cycles in  
39 catalyst performance optimization. To harvest the potential of such approaches, a homogeneous  
40 mixture of relevant elements in the material is required. Generally, however, production of  
41 multimetallic nanomaterials has been limited to various forms of heterostructures due to the  
42 often-large miscibility gaps that exist for various metal systems whenever conventional routes  
43 are used yielding thermodynamic phase-segregated products.<sup>[9]</sup> This limits the added value of  
44 a multicomponent system in reaction optimization to concurrent catalysis.<sup>[10]</sup>

45 Recently, various non-equilibrium methods have been established that allow for the mixing of  
46 the elemental constituents at the nanoscale such as spark ablation, carbo-thermal shock  
47 synthesis and laser deposition.<sup>[11],[12],[13],[14],[15]</sup> Unfortunately, these techniques require  
48 extremely harsh conditions ( $\Delta T > 900$  °C) with subsequent quenching to yield the non-  
49 equilibrium states rendering the possibility to control the exposed crystal facet improbable. As  
50 it has been shown that crystal facets play an important role in controlling reaction pathways,<sup>[16]</sup>  
51 allowing for mixing of various elements at the nanoscale congruent with shape control would  
52 offer tremendous insight in the fundamentals of various catalytic processes. One such example  
53 is the electrochemical reduction of CO<sub>2</sub> (CO<sub>2</sub>RR), in which convoluted facet and electronic  
54 effects induced by elemental mixing have been shown. For instance, facet-dependence in  
55 CO<sub>2</sub>RR has been demonstrated in Cu single- and nanocrystals (NCs), e.g., Cu(111), Cu(110)  
56 and Cu(100) facets are selective for CH<sub>4</sub>, oxygenates and C<sub>2</sub>H<sub>4</sub>, respectively.<sup>[17],[18],[19],[20]</sup>  
57 Instead, upon the introduction of Ag adatoms in Cu(100) single crystals, the selectivity  
58 switches towards oxygenates.<sup>[21],[22]</sup> Further, three-component Cu based systems such as Ag-  
59 Ru-Cu have recently been reported as the state-of-the-art in the conversion of CO to n-  
60 propanol.<sup>[23]</sup>

61 With the opportunities for combined component and facet control in mind, we revisited the  
62 well-known colloidal galvanic replacement reaction. Generally, this method yields various  
63 heterostructures, i.e., thermodynamic products.<sup>[24]</sup> However, by introducing a kinetic barrier,

we were able to trap kinetic non-equilibrium nanosurface alloy (NSA) structures (**Figure 1**). In here, a homogeneous mixture of multiple components is achieved in a few monolayers thin shell surrounding a pure core. We used the Cu-Ag system as a proof-of-concept to overcome immiscibility for its positive heat of mixing at nearly any composition.<sup>[25]</sup> Generally, syntheses of Cu-Ag yields phase-segregated materials such as core-shell, core-cluster, and nanodimers,<sup>[26],[27],[28],[29]</sup> and, with a few exceptions, alloys that lack size and shape control.<sup>[21],[30],[31]</sup> We show that with our simple yet elegant low-temperature, thin film-based galvanic replacement method, anisotropic (e.g., tetrahedral (Th), cubic (C) and truncated octahedral (TOh)) non-equilibrium multimetallic structures can be synthesized with controlled size, shape, and (surface) composition. Further, we demonstrate that this non-equilibrium synthesis is applicable for a broad library of binary and ternary surface alloys, as evidenced in our Cu-M systems with M = Pd, Au and Ag-Pd.

Using Cu-Ag NSAs as model catalysts, we investigate the effect of crystal facet on the performance of bimetallic catalysts in CO<sub>2</sub>RR, due to its significant structural sensitivity.<sup>[21],[30]</sup> We find that both Cu-Ag(100) and Cu-Ag(111)/Cu-Ag(100) faceted C- and TOh-NSAs show a high faradaic efficiency (FE) of ~58% towards C<sub>2</sub><sup>+</sup> products, where TOh-NSAs show particular selectivity towards liquid fuels, including acetate, acetaldehyde, ethanol and n-propanol. We confirm the expected surface segregating tendencies of the Cu-Ag system<sup>[32]</sup> by various ex-situ electron microscopy techniques and correlate it to the observed dynamic changes in the product distributions. We demonstrate that the phase stability of the Cu-Ag system can be improved by introducing a ternary miscible element (i.e., Pd). Further, using a supervised machine-learning approach, we predict high C<sub>2</sub><sup>+</sup> selectivity and phase stability for the Cu<sub>79</sub>Ag<sub>16</sub>Pd<sub>5</sub> alloy and verify these predictions through nonequilibrium synthesis and electrochemical tests. This low-temperature non-equilibrium synthesis provides unprecedented control over the facet and composition of multimetallic nanomaterials and offers a range of binary and ternary surface alloy catalysts for energy applications.

90

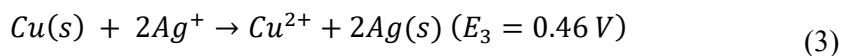
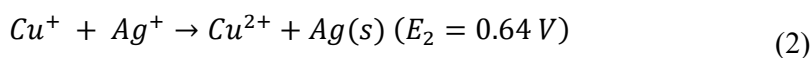
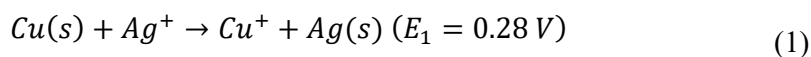
## 91 **2. Results and Discussion**

### 92 **2.1 Low-temperature non-equilibrium synthesis of Cu-Ag anisotropic nanosurface alloys**

93 A typical galvanic replacement process for synthesizing structurally controlled Cu-Ag NCs  
94 consists of two steps: (1) synthesis of anisotropic Cu NCs, and (2) subsequent galvanic

exchange of Cu with Ag salt. This two-step synthesis allows a free choice of seed shape in the first step, and in view of this, Th-, C-, and TOh-Cu NCs were synthesized with a colloid synthesis method (**Figure S1**).<sup>[33]</sup> In the second step, we differentiate between a conventional galvanic replacement reaction and a non-equilibrium one. For the conventional galvanic replacement reaction, Cu crystals are well dispersed in the solution under magnetic stirring. Thus the reaction is thermodynamically controlled, where the rapid exchange rates and the positive heat of mixing of Cu seeds and Ag<sup>+</sup> ions lead to the formation of individual Ag domains at the particle surfaces, preferentially at the corners and edges (**Figure S2**).<sup>[26],[27],[28]</sup> For details on the thermodynamics and kinetics of the synthesis see **Figure S3** and **Note S1** of the Supporting Information. Instead, for the non-equilibrium synthesis, anisotropic seeds are kept undisturbed at the bottom of the vial and homogeneously-distributed Ag atoms are incorporated in the Cu lattice as the kinetic product. An overview of the conventional and non-equilibrium synthesis is presented in **Figure 1A**. **Figure 1B** shows the randomly-distributed solute in the Cu-based NSAs. Further details on the non-equilibrium synthesis can be found in the protocol see **Materials and Methods**, **Figure S4**, and **Note S1**. In addition, homogeneous Cu-Ag NSAs were also obtained in the scaled-up nonequilibrium synthesis (**Figure S5**), demonstrating the controllability and practicality of this method.

The key to the successful synthesis of NSAs is the precise control over the mass transport of the reactants. In the Cu-Ag system for example, reaction (1)-(3) can take place spontaneously.



If the replacement process proceeds through reaction (1), each Ag<sup>+</sup> replaces exactly one Cu atom. However, if reaction (2) directly follows reaction (1), or Cu is twice oxidized in a single step via reaction (3), two Ag atoms are exchanged per Cu atom, leading to a local accumulation of Ag. Reaction (2) and (3) require two Ag<sup>+</sup>, i.e., a high local concentration of Ag<sup>+</sup>, to occur. Instead, reaction (1) can readily occur at a low Ag<sup>+</sup> concentration. Therefore, through confining the Cu seeds in a thin-film and restricting the Ag<sup>+</sup> to diffuse to the depletion zone, the non-equilibrium synthesis ensures the predominant occurrence of reaction (1). Since each atom of the Cu facet is equally likely to be replaced, it is a random event. Although the surface energies of the corner and edge atoms are slightly higher, the low Ag<sup>+</sup> concentration restricts their

preferential exchange as stoichiometric replacement does not improve the degree of undercoordination.<sup>[34],[35]</sup> Finally, their small relative surface abundance limits their overall contribution to the reaction.<sup>[35]</sup> This eventually leads to the formation of Cu-Ag NSAs as kinetic products, rather than thermodynamically favorable phase-segregated products. This mechanism is supported by the kinetic study shown in **Figure S6**, where the non-equilibrium synthesis shows a much lower reaction rate compared to the conventional synthesis. In addition, we show that by accelerating reaction (2) (i.e., introducing additional Cu<sup>+</sup> ions in the reaction mixture), the kinetic products can be converted into the thermodynamic heterostructures (**Figure S7**), further supporting the criticality of controlling the reaction kinetics.

The morphology of anisotropic Cu-Ag NSAs with different shapes was studied with transmission electron microscopy in bright-field mode (BF-TEM, **Figure 2A-C**). The well-defined tetrahedral, cubic, and truncated octahedral structure indicate that the original Cu NCs structures are well preserved during Ag deposition. A homogeneous distribution of Ag at the surface of the Cu NCs was confirmed by energy dispersive X-ray spectroscopy (EDXS) in scanning transmission electron microscopy (STEM) (**Figure 2D-F**). Using the previously developed single particle-inductively coupled plasma mass spectrometry (SP-ICP-MS) method, we probed the ensemble representative composition distributions (**Figure 2G-I**).<sup>[33]</sup> This method enables the determination of the elemental composition of individual NPs with ensemble representative statistics, and with the aid of further geometrical modelling, surface compositions can be extracted from the obtained elemental distributions. Independent of the facet, a nearly 1:1 ratio between the number of atoms of the outermost Cu monolayer (ML) and the total number of Ag atoms present in the particles was determined, further corroborating the limit of the presence of Ag to the outermost layers of the Th-, C- and TOh-Cu-Ag NSAs (**Figure 2G-I**). We determine that an equivalent of 1.1-1.5 MLs of Ag have been deposited (as based on the 1<sup>st</sup> Cu ML, see **Figure S8**, **Table S2** and **Note S2**). Further, by determining the surface composition with XPS (Cu<sub>0.91</sub>Ag<sub>0.09</sub>), we estimate a diffusion of Ag into the Cu lattice of up to 11 MLs in the C-Cu<sub>0.97</sub>Ag<sub>0.03</sub> NSA (**Figure S9** and **Table S3**).

Further, we probed the valence band spectra of the as-prepared NSAs by X-ray photoemission spectroscopy (XPS) to verify whether an alloy or segregated phases was formed, as previous studies have shown that charge transfer from Cu to Ag occurs when forming surface

alloys.<sup>[36],[37]</sup> It is shown that the center-of-gravity of the Cu-Ag NSA valence bands shift towards the Fermi level, indicating charge-transfer, corroborating the surface alloy nature (**Figure 3A**, see **Materials and Methods** for details).<sup>[38]</sup> Further, we performed X-ray absorption spectroscopy (XAS) under inert conditions at the Ag K-edge to probe the atomic structure of the Cu-Ag NSA. The  $k^3$ -weighted extended X-ray absorption fine structure (EXAFS) spectrum excluded the presence of Ag-O bonds, confirming the metallic nature of the NSA, which is expected based on the principles of the galvanic replacement reaction (**Figure 3B**). Further, fitting of scattering paths in the first coordination shell indicated the presence of both Ag-Cu as well as Ag-Ag bonds with high degree of undersaturation. This suggests the presence of single atoms or at most groups of a few Ag atoms (3-8) bonded to undercoordinated Cu sites, i.e., the surface, corroborating the disordered nature of the NSA surface.<sup>[39]</sup> Moreover, the Cu-Ag NSA X-ray absorption near-edge structure (XANES) spectrum showed a shift of the absorption edge to lower energy compared to Ag foil, indicating charge-transfer from Cu to Ag in agreement with the valence band spectra (**Figure S10**). For details on the experimental procedure and fitting parameters, see **Materials and Methods**, and **Table S4**.

To determine the absolute penetration depth of the Ag atoms, we designed a microtomy based experiment<sup>[40]</sup> in which the top and bottom face of the C-Cu-Ag NSA was removed with a diamond knife (**Figure S11**). This resulted in a 2D particle consisting of a Cu-Ag random alloy outer ring surrounding a pure Cu core (**Figure 4**). Atomic resolution imaging and EDXS performed on an aberration-corrected STEM<sup>[41]</sup> reveal that Ag is only present in the first 6 MLs of the NSA (**Figure 4B-D**). A refit of the SP-ICP-MS surface atom distribution using the revealed Ag penetration depth, puts the average surface composition at 21.3 at.% Ag (**Note S2**). Notably, the measured composition surpasses the bulk solid solubility of Ag in Cu at room temperature by at least two orders of magnitude, highlighting the importance of this method in overcoming the inherent immiscibility of bimetallic materials.<sup>[42]</sup> Further, we demonstrate that the surface composition of the Cu-Ag NSA can be tailored by controlling the reaction time of the non-equilibrium synthesis (**Figure 3A** and **Table S3**). In addition, we studied the thermal stability of our metastable NSA using ex situ TEM at identical location of the specimen (**Figure S12**). The results reveal that the C-Cu-Ag NSA remained stable up to 200 °C, which is ~25 °C higher than the reported stability temperature of Ag<sub>0.60</sub>Cu<sub>0.40</sub> solid solution thin films.<sup>[43]</sup>

Since the low-temperature non-equilibrium synthesis is based on the galvanic replacement reaction, it should be applicable to different systems as long as there is an appropriate overall

cell potential.<sup>[24],[44]</sup> With this in mind, Cu-Au, Cu-Pd and Cu-Pd-Ag NSAs were successfully synthesized using the same reaction parameters as those for Cu-Ag NSAs (see **Materials and Methods, Figure 1, Figure S13, and Figure S14**). We would like to emphasize that for a seed with a lower standard reduction potential than Cu, a wider range of exchangeable metals should be accessible. Nonetheless, excessively large potential differences may result in a significant increase in heat of exchange, potentially compromising control over the resulting structure. Therefore, the overall cell potentials investigated in this study (+280 mV to +1160 mV for the Cu-Ag and Cu-Au systems, respectively) represent a safe range for synthesizing NSAs.<sup>[45]</sup> Finally, we propose that our synthesis methodology can be extended to produce multicomponent systems beyond three-elements such as high-entropy NSAs by sequentially pairing metals of progressively increasing overall cell potentials.

## 2.2 Facet dependent selectivity of Cu-Ag NSAs in CO<sub>2</sub>RR

We further tested our anisotropic Cu-Ag systems in the CO<sub>2</sub>RR to demonstrate the low-temperature non-equilibrium synthesis as a screening platform for anisotropic alloyed multimetallic electrocatalysts (**Figure 5**). We first benchmarked our system by testing the C-, Th-, TOh-Cu single element NCs at a constant potential (−1.1 V vs RHE) in 0.1 M KHCO<sub>3</sub> in an H-cell (**Figure 5A**). Indeed, we could confirm that our faceted Cu seeds followed the same general trend as found in the literature: C-Cu(100) NCs are mostly ethylene selective (FE of 31%),<sup>[18],[46]</sup> Th-Cu(111) is mostly methane selective (29%),<sup>[47]</sup> and TOh-Cu(100)/Cu(111) shows a slightly higher selectivity towards liquid fuels such as acetate and ethanol etc. (14%).<sup>[48]</sup> Then, to test if any Ag introduced using the galvanic replacement reaction was catalytically active, we synthesized Ag-Cu NPs as control samples and tested their CO<sub>2</sub>RR activity (**Figure S15**). By extending the reaction time and increasing the Ag<sup>+</sup> concentration in the non-equilibrium synthesis, near-to-complete conversion of the anisotropic Cu NCs to isotropic Ag NPs was achieved (>96 at.% Ag, see **Materials and Methods** for details, **Figure S15A-D**). Upon applied potential, it is shown that CO is the majority product (FE >59%) independently of the shape of the seed (**Figure S15D**), confirming the activity of the introduced Ag, which is a well-known CO evolving catalyst.<sup>[49]</sup>

With the pure NCs benchmarked and the Ag activity confirmed, we turn to the investigation of the facet effect in bimetallic Cu-Ag alloys. To deconvolute facet from composition effects, we tested specifically those Cu-Ag NSAs of equal composition in the CO<sub>2</sub>RR (C-, Th, and TOh-

Cu<sub>0.97</sub>Ag<sub>0.03</sub>, **Figure 5B**). Independent of the facet, a selectivity shift from C<sub>1</sub> products to C<sub>2+</sub> could be noted upon the introduction of Ag with the starkest shift for the Th-Cu-Ag NSA (C<sub>2+</sub> FE from 15% to 40%, **Figure 4C**). Further, a significant amount of acetaldehyde could be detected in the catholyte (FE >9%, **Figure 5C-D**, **Table S5**, **Figure S16**), which is absent for the pure Cu samples.<sup>[50]</sup> The selectivity towards ethanol improved as well, whereas the FE towards ethylene increased only marginally (**Figure 5C-D**). Therefore, we conclude that Ag adatoms in Cu surfaces favor C<sub>2+</sub> products (especially oxygenate) over C<sub>1</sub> products, which is in agreement with the results reported for Cu-Ag(100) bulk single-crystal surface alloys.<sup>[21]</sup> Notably, the TOh-Cu-Ag NSA showed the strongest gains in selectivity towards liquid fuels with acetaldehyde, ethanol and n-propanol approaching double digits (9%, 16% and 9%, respectively, **Table S4**). To our knowledge, no Cu-Ag-based NP system exists that surpasses, at comparably low overpotential in the H-cell, the 35% overall FE towards C<sub>2+</sub> liquid fuels.

The remarkable preference for C<sub>2+</sub> liquid fuels (e.g., acetate, acetaldehyde, ethanol and n-propanol) over ethylene upon the introduction of Ag in both Cu(111) and Cu(100) faceted crystals can be attributed to the electronic tuning of the active site, which is distinct from tandem-based catalysts.<sup>[51],[52],[53]</sup> The electronic nature of the catalyst surface determines the binding strength of key intermediates and can thereby greatly influence the selectivity.<sup>[54]</sup> For transition metals, the binding strength is dictated by the interaction of their d-band with an adsorbate. The closer the d-band center lies to the Fermi level, the stronger the adsorbate binding.<sup>[55]</sup> Stronger binding of \*CO as compared to pure Cu due to charge transfer effects enhances the C-C coupling rate and thus the selectivity for C<sub>2+</sub> products for Cu-Ag NSAs (**Figure 3A** and **Figure S17**). This also explains the larger enhancement factor of C<sub>2+</sub>/C<sub>1</sub> for Cu-Ag(111) vs Cu-Ag(100) surfaces: the charge-transfer for Th-Cu<sub>0.97</sub>Ag<sub>0.03</sub> and C-Cu<sub>0.97</sub>Ag<sub>0.03</sub> is 100 and 90 meV, respectively. The reason for the more pronounced production of liquid fuels over ethylene is two-fold. First, charge-depleted Cu has been shown to favor C<sub>2+</sub> products,<sup>[29],[37]</sup> especially oxygenates.<sup>[56]</sup> Second, the weak hydrogen adsorption strength of Ag results in lower \*H coverage,<sup>[8]</sup> which limits further hydrogenation and steers selectivity towards oxygenates. This is in agreement with observations for tandem Cu-Ag catalysts<sup>[57]</sup>, and bulk surface alloys.<sup>[21],[22]</sup>

### 2.3 Phase-segregation induced selectivity shift

Since the Cu-Ag bimetallic system has a strong tendency for surface segregation,<sup>[32]</sup> which may affect the catalytic performance, we performed a constant potential CO<sub>2</sub>RR experiment to



evaluate the stability of our NSAs (**Figure 6, Figure S18**). For each anisotropic Cu-Ag NSA (Th-, C-, and TOh-Cu<sub>0.97</sub>Ag<sub>0.03</sub>), a decreasing FE for liquid fuels could be observed with the fastest decay observed for the TOh-Cu<sub>0.97</sub>Ag<sub>0.03</sub> (from 35% to 25% in a matter of minutes). This was accompanied by an increase in FE of H<sub>2</sub>. Also, the geometrical partial current densities pointed towards a decaying liquid fuel activity accompanied by an increase in the H<sub>2</sub> evolution reaction (HER, **Figure S19**).

To confirm phase-segregation as the culprit for the loss in selectivity, we analyzed the spent catalyst using TEM (**Figure 6C1-3**). Strong contrasted extrusions at the particle surface could be discerned for the Th-, C- and TOh-Cu-Ag NSA after CO<sub>2</sub>RR, which were absent in the pristine samples (**Figure 6B1-3**). The presence of extrusions at the particle surfaces of the spent catalysts could be confirmed with the scanning electron microscopy (SEM), while the extrusion for the control C-Ag<sub>0.97</sub>Cu<sub>0.03</sub> NPs, which lacked the tendency of phase segregation, can be excluded (**Figure S20 and S21**). We assign these extrusions to the mobile Ag phase. Since phase-segregation results in Ag domain formation predominantly at the most undercoordinated sites, i.e., edges and corners (**Figure S11**), which are most selective for C-C coupling and especially the production of oxygenates,<sup>[47],[52]</sup> we argue that phase-segregation blocks those active sites explaining the progressive loss of liquid fuels selectivity over time (**Figure S18**). We, therefore, stress the importance of monitoring all products of the CO<sub>2</sub>RR and the sample at least *ex situ* when testing metastable catalysts. Fast adsorbate-induced changes to the surface chemistry may otherwise cloud interpretations of the intrinsic activity.

## **2.4 Theory-guided Cu-Ag-Pd catalyst selection for stable C<sub>2+</sub> liquid fuel electrosynthesis**

Based on the wide applicability of our low-temperature non-equilibrium synthesis, we set out to improve the stability of the metastable Cu-Ag NSAs using metals that are miscible with Cu. Limited only by the difference in standard reduction potentials of the metals and the solubility of the salt in the reaction medium, a range of candidates (e.g., Rh, Pt, Pd, and Au) could be selected.<sup>[58]</sup> Previously, we have shown in the Cu-Ag-Pd system that Ag could be selectively exchanged by Pd<sup>2+</sup> while Cu remained untouched by choosing the right metal salt precursor.<sup>[33]</sup> This offers an opportunity to gradually introduce Pd into the Cu-Ag NSA and to explore the effect of Pd on the phase stability and the CO<sub>2</sub>RR performance. However, it is worth to note that Pd is highly active for HER,<sup>[59]</sup> therefore, the ratio of Pd and Ag needs to be precisely tuned to optimize the performance.

Using a supervised machine-learning algorithm reported previously,<sup>[8]</sup> but trained with a data set of \*CO and \*H adsorption energies over ternary Cu-Ag-Pd surfaces simulated with density functional theory (DFT), compositions with high CO reduction reaction (CORR) selectivity (i.e., selectivity towards CH<sub>4</sub> and C<sub>2+</sub> products) and low H<sub>2</sub> selectivity could be predicted (**Figure 7A**). CORR selectivity is here predicted as the proportion of surface sites on disordered face-centered cubic (111) surfaces with stronger \*CO adsorption than on the reference Cu(111) surface. Selectivity for reducing CO<sub>2</sub> and subsequently CO (i.e., by suppressing H<sub>2</sub> formation) is predicted as the proportion of sites with weaker \*H adsorption than on Cu(111). Prediction of adsorption energies was achieved on arbitrary surface sites using a linear regressor (**Figure S22, Table S7**). In **Figure 7A**, each data point represents a predicted CO<sub>2</sub>RR/CORR selectivity for a specific composition of the ternary alloy. With the low-temperature non-equilibrium synthesis, such NSAs could be synthesized and tested in CO<sub>2</sub>RR (**Figure 7B**). Calculations predicted good C<sub>2+</sub> selectivity for Ag:Pd of 1:3 whereas the inverse would suffer from H<sub>2</sub> production. Experimentally, enhanced liquid fuel production could be observed for the Cu<sub>79</sub>Ag<sub>16</sub>Pd<sub>5</sub> NSA whereas high HER activity was observed for the sample with 16 at.% Pd (**Figure 7C**). The good agreement between the predicted and the experimentally determined CORR/CO<sub>2</sub>RR selectivity confirms the validity of the machine-learning based approach in predicting component-selectivity relations in alloy systems.

### 3. Conclusion

Multicomponent congruently mixed nanoparticles are well underway in playing a dominant role in the energy research field. To fully harvest the catalytic potential of such systems, advanced syntheses must not only overcome miscibility gaps, but also enable shape and composition control to deconvolute their effects in catalysis. To this end, we developed a low-temperature non-equilibrium synthesis method and demonstrated its capability and generality by producing anisotropic (e.g., cubic, tetrahedral, and truncated octahedral) multimetallic nanosurface alloys of up to three components (e.g., Cu with Ag, Pd, and Au). Further, we utilized our shape-controlled Cu-Ag NSAs as a model catalytic platform for CO<sub>2</sub>RR, elucidated the structure-performance relationships, and showed improved selectivity towards C<sub>2+</sub> liquid fuels compared with their monoelemental counterparts. Finally, guided by machine learning, we synthesized Cu-Ag-Pd NSAs with high C<sub>2+</sub> selectivity and phase stability. With a large number of multimetallic compositions and systems accessible as well as the added facet control, we expect our low-temperature non-equilibrium synthesis to be of great advantage for researchers seeking nanomaterials of specific spatial atomic arrangements.

316

## 317 **4. Materials and Methods**

### 318 **4.1 Chemicals**

319 The following chemicals and solvents were acquired from Sigma-Aldrich: copper bromide  
320 99.99% (CuBr), palladium chloride 99% (PdCl<sub>2</sub>), gold chloride (AuCl<sub>3</sub>), nitric acid 70%  
321 (HNO<sub>3</sub>), trioctylphosphine oxide 99% (TOPO), trioctylphosphine 99% (TOP), and oleyl  
322 amine 70% (OAm). Anhydrous ethanol 95% was purchased from ACROS organics (EtOH)  
323 and anhydrous toluene 99.8% from Alfa Aesar. Lastly, silver nitrate (AgNO<sub>3</sub>) 99.9995% was  
324 obtained from Puratrem. All chemicals were used as received without any further purification.

### 325 **4.2 Non-equilibrium synthesis**

326 The low-temperature non-equilibrium synthesis is inspired by the protocol from Lee et al.<sup>[27]</sup>  
327 Typically, 4 mg of anisotropic Cu NPs synthesized using a Schlenk-line (**Figure S1**) dispersed  
328 in a minimal amount of anhydrous toluene (19 mg/mL based on ICP-OES) were added to a 10  
329 mL glass vial in the glove box creating a NP thin film, to which 3.5 mL of degassed OAm were  
330 added carefully without disturbing the film (non-equilibrium synthesis). Further, 0.5 mg of dry  
331 AgNO<sub>3</sub> were added to 1.5 mL of degassed OAm and dissolved at 50 °C using an oil bath to  
332 prevent homogeneous nucleation (Cu:Ag equals 21:1, **Figure S23**). Then, using a clean  
333 syringe, the Ag salt solution was dropwise added to the reaction vial. For the C-Cu-Ag NSAs,  
334 the reaction mixture was then allowed to react at 80 °C for 1 or 5 min, for TOh-Cu-Ag at 80 °C  
335 for 5 min, and for Th-Cu-Ag at 50 °C for 1 min. For the isotropic Ag-Cu NPs, the Cu:Ag ratio  
336 was increased to 1:3 and the reaction time was extended to 24 hrs to ensure the near-to-  
337 complete exchange (**Figure S15**). In each case, the reaction was quenched with anhydrous  
338 toluene and washed with the same solvent. C-Cu-Au and C-Cu-Pd NSAs were obtained by  
339 replacing AgNO<sub>3</sub> with AuCl<sub>3</sub> or PdCl<sub>2</sub> and increasing the dissolution temperature to 80 °C in  
340 case of Cu-Pd and reducing the reaction temperature to 50 °C in case of Cu-Au, but otherwise  
341 keeping all other conditions constant. Using C-Cu-Ag NSAs to react with a Pd salt solution,  
342 C-Cu-Pd-Ag NSAs could be obtained as well. For details on the conventional synthesis, see SI  
343 **Note S1**.

### 344 **4.2 Ex situ TEM measurements**

345 A monolayer of C-Cu-Ag NSAs was deposited on thermally resistant Si<sub>3</sub>N<sub>4</sub> grids purchased  
346 from Ted Pella Inc. and placed in a MILA-5000 rapid thermal annealer. After flushing the gas

tight system with N<sub>2</sub> for 30 min. The temperature was increased to 100 °C with ramp of 50 °C·s<sup>-1</sup> and kept at that temperature for 30 min, after which the reaction was quenched by flushing again with N<sub>2</sub>. After the reaction, the stability of the NSA was investigated using TEM performed on identical sample locations. The experiment was further repeated for 200 °C, 300 °C and 400 °C to monitor the stability. After the final annealing experiment, STEM-EDXS (on identical locations) was performed to confirm the mobility of the Ag phase.

### 4.3 Cathode preparation

Belt-shaped pieces of Toray TGP-60r carbon paper were cut out with a geometrical surface area of 0.5 cm<sup>2</sup>, to which 0.8 mg·cm<sup>-2</sup> worth of the anisotropic Cu NCs, Cu-Ag, Cu-Ag-Pd NSAs or isotropic Ag-Cu NPs dispersed in toluene were added using drop casting in the glovebox. Finally, 20 µL of 0.83 wt% Nafion dispersed in *iso*-propanol were added as binder.

### 4.4 Characterization

**Electron microscopy (EM).** SEM images were acquired using a Thermo Scientific Teneo. TEM images were acquired with a Thermo Scientific Tecnai-Spirit operated at 120 kV in bright-field mode. The microscope was equipped with a Gatan Orius charge-coupled device (CCD) camera and Digital Micrograph for imaging. Samples were drop-casted on Au grids (400 mesh) from Ted Pella Inc. with ultrathin carbon film, which were washed with ethanol before and after drop-casting. Ni based grids were used for Au containing samples. Scanning transmission electron microscopy (STEM) was performed using a double Cs-corrected Thermo Scientific Titan-Themis 60-300 and Tecnai-Osiris at an acceleration voltage of 200 kV. These microscopes are equipped with high-brightness X-FEG and Super-X EDX systems, comprising four silicon drift detectors and Velox acquisition software. STEM images were acquired in the high-angle annular dark-field (HAADF-STEM) condition. Atomic resolution images were obtained using a beam current of 200 pA. To study the penetration depth of the Ag inside the particle, some samples were embedded in the G2 resin and sliced to 40 nm thick slices by ultramicrotomy using a Leica EM FC7 machine (equipped with a Diatome cryo-knife 35° angle) at the room temperature and with a cutting speed of 0.2 mm s<sup>-1</sup>. Ultramicrotomed slices were deposited on an ultra-thin carbon support grid for TEM and EDXS.

**X-ray photoelectron spectroscopy (XPS).** XPS was performed on a Kratos Axis Supra system (analysis chamber base pressure  $1 \times 10^{-9}$  mbar), using a monochromated Al K<sub>α</sub> (1486.61 eV) X-ray source at a nominal power of 225 W. A pass energy of 20 eV was used for acquiring all core-level and Auger electron spectra, as well as the X-ray excited valence band spectra. The

binding energies (BEs) were referenced to Au 4f<sub>7/2</sub> at 83.95 eV. The samples were drop-casted on a gold foil in a N<sub>2</sub> glovebox and transferred for measurement without exposure to air. No charge compensation was required as the samples were conductive.

**Inductively coupled plasma – optical emission spectroscopy (ICP-OES).** The concentration of the digested NP solutions was determined with an Agilent 5110 ICP-OES with a VistaChip II CCD camera. The NPs were digested overnight in 2% HNO<sub>3</sub> and filtered with 400 µm pore size Ultrapore nylon filters. The calibration curves were obtained through the preparation of a dilution series of elemental standards obtained from Sigma Aldrich.

**Inductively-coupled plasma mass spectrometry (ICP-MS).** Single-particle elemental analysis of the Th-, C- and TOh-Cu-Ag NSAs was achieved with a NexION 350D ICP-MS instrument from PerkinElmer operated in continuous data acquisition mode. Calibration of the transport efficiency ( $\eta_t$ ) was achieved with Au NPs standards 30, 50 and 80 nm purchased from PerkinElmer at a NP number concentration of ~50,000 NPs mL<sup>-1</sup>.

**X-ray absorption spectroscopy (XAS).** XAS measurements at the Ag K-edge were performed at the SuperXAS beamline at the Swiss Light Source (Villigen, Switzerland). The measurements were done with Pt-coated collimating mirror at 2.9 mrad, Si(111) channel-cut monochromator, Pt-coated toroidal focusing mirror. The beam size on the sample was 300×300 µm. The beam intensity was monitored with three 15 cm-long ionization chambers filled with 1 bar Ar and 1 bar N<sub>2</sub>. The sample spectrum was measured with a 5 element SDD detector (SGX) and normalized to the intensity of the incident beam. The Ag foil was mounted between the second and the third ionization chambers and measured simultaneously with the sample, for precise energy calibration. No changes to the sample were observed during the measurement.

#### 4.5 Density Functional Theory simulations

126 atop \*CO and 160 face-centered cubic (fcc) threefold hollow \*H adsorption energies were simulated on fcc (111) surfaces of randomly generated, periodically repeated surface slabs sized 3×3×5 atoms with 10 Å of vacuum above and below the slab. The lattice constants were set to the average of the constituent elements in the top layer.<sup>[60]</sup> Simulations were performed in the GPAW code<sup>[61],[62]</sup> version 22.1.0 and the atomic simulation environment (ASE)<sup>[63]</sup> version 3.22.1 for atomic manipulations. Energies were computed using the RPBE exchange-correlation functional<sup>[64]</sup> using a plane wave basis set with an energy cutoff of 400 eV. The

Brillouin zone was sampled on a 4×4×1 uniform Monkhorst-Pack grid of k-points, and atoms were relaxed to a force below 0.075 eV/Å.

## **5. Data availability**

All data are available in the paper and its Supplementary Information. Source data that support the findings of this study are available from the corresponding authors upon reasonable request.

## **6. Code availability**

DFT simulated atomic structures have been made freely available at [nano.ku.dk/english/research/theoretical-electrocatalysis/katlab/co2-reduction-on-ag-cu-pd/](http://nano.ku.dk/english/research/theoretical-electrocatalysis/katlab/co2-reduction-on-ag-cu-pd/).

## **7. Acknowledgement**

This research was supported by Swiss National Science Foundation (Ambizione Project PZ00P2\_179989). Mo Li acknowledges the financial support from China Scholarship Council (Grant No. 201506060156). Jack K. Pedersen and Jan Rossmeisl acknowledge support from the Danish National Research Foundation Center for High Entropy Alloy Catalysis (CHEAC) DNRF-149. Laure Menin and Natalia Gasilova of the Mass Spectrometry and Elemental Analysis Platform (MSEAP), Institute of Chemical Sciences and Engineering (ISIC), Basic Science Faculty (SB), École Polytechnique Fédérale de Lausanne (EPFL) Valais/Wallis, Energypolis, Sion, Switzerland, are acknowledged for their facilitation of the ICP-MS/OES measurements. Sumant Phadke is acknowledged for his assistance in the preparation of the capillaries.

## **8. Author contributions**

C.D.K., W.L. and A.Z. conceptualized the project. W.L. and A.Z. supervised the project. C.D.K. developed the synthesis of the catalysts, performed the electrochemical tests, catalyst characterizations, and the related data processing. E.O. performed the HRTEM characterizations and the related data processing. J.Z. performed the SEM characterizations, assisted the electrochemical tests and product analysis. M.L. performed the XPS analysis. O. S. performed the XAS measurement and related data treatment. J.K.P performed the DFT simulation with supervision from J.R. C.D.K and W.L. co-wrote the manuscript. All the authors discussed the results and revised the manuscript.

## **9. Ethics declarations**

**Competing interests:** The authors declare no competing interests.

## 10. Additional Information

**Supplementary information** The online version contains supplementary material available at <https://doi.org>

**Correspondence and requests for materials** should be addressed to Wen Luo.

## 11. Figures legends/captions

**Figure 1. The conventional and non-equilibrium synthesis.** (A) Schematic illustration of the conventional and non-equilibrium galvanic replacement reaction, where phase-segregated heterostructures and homogeneous surface alloys were formed, respectively. (B) STEM-EDXS elemental maps of Cu, Ag, Pd and Au in cubic Cu-Ag, Cu-Ag-Pd, Cu-Pd and Cu-Au NSAs prepared by using the non-equilibrium method showing the random nature of the added component(s) and increased intensity at the NP edges.<sup>[33]</sup>

**Figure 2. Structural and compositional analysis of anisotropic Cu-Ag NSAs.** (A-C) BF-TEM image of the Th-Cu-Ag NSA (A), C-Cu-Ag NSA (B), and TOh-Cu-Ag NSA (C). (D-F) STEM-EDXS elemental maps of the Th-Cu-Ag NSA (D), C-Cu-Ag NSA (E), and TOh-Cu-Ag NSA (F). STEM-EDX elemental maps depict Cu in orange and Ag in turquoise. A random distribution of Ag in the Cu surface and the increased intensity at the particle edges can be observed from the maps. Note that the ability to determine Ag enrichment at the particle surface via the elemental map is limited by the particle orientation with respect to the beam and the fact that the distribution is a 2D projection of a 3D volume. (G-I) Distribution of the number of atoms in the surface of the Th-CuAg NSAs (G), C-CuAg NSA (H), and TOh-CuAg NSA (I) for N single particles ( $N > 500$ ), as determined with SP-ICP-MS. The deposited amount of Ag on Th-CuAg, C-CuAg, and TOh-CuAg NSAs are equivalent to 1.4, 1.1 and 1.5 ML, respectively. ICP-OES determined particle bulk composition are Th-Cu<sub>0.97</sub>Ag<sub>0.03</sub>, C-Cu<sub>0.97</sub>Ag<sub>0.03</sub>, TOh-Cu<sub>0.97</sub>Ag<sub>0.03</sub>, respectively.

**Figure 3. XPS and XAS characterization of anisotropic Cu-Ag NSAs.** (A) Valence band spectra of pure Cu and Ag references and three C-Cu-Ag particles synthesized at different reaction times using the non-equilibrium synthesis (1, 5 min and 2 hrs). The center-of-gravity of the valence band construed exactly half the area-under-the-curve of the spectra (denoted by the dotted line), which was determined by numerically integrating the spectra with fixed bounds at 0 and 9 eV, respectively. The shift of the valence band towards the Fermi level as compared to pure Cu confirms the random alloy nature of the C-Cu<sub>0.99</sub>Ag<sub>0.01</sub> and C-Cu<sub>0.97</sub>Ag<sub>0.03</sub>

NSAs as charge-transfer occurs from Cu to Ag. Instead, for a phase-segregated material (C-Cu<sub>0.13</sub>Ag<sub>0.87</sub>), the valence band spectrum is a linear combination of the Cu and Ag reference spectra showing no charge-transfer. The asterisk (\*) in (A) indicates the valence band spectra of the same ensemble of particles indicated in **Figure 2H**. (B)  $k^3$ -weighted EXAFS spectrum of the Ag K-edge of the C-Cu<sub>0.99</sub>-Ag<sub>0.01</sub> NSA (purple) and respective fit (dashed black). The presence of highly undercoordinated Ag-Cu and Ag-Ag bonds (coordination number of  $= 1.1 \pm 0.3$  and  $2.7 \pm 0.9$ , respectively) suggest single atoms or at most groups of a few Ag atoms (3-8) bonded to the outermost layer(s) of the NSA. The Ag-Cu (red) and Ag-Ag (blue) scattering paths indicated in the plot were used for the fit.

**Figure 4. Determination of the penetration depth of Ag in the NSAs.** (A) High-resolution STEM-HAADF image of a 40 nm slice of a C-Cu<sub>0.97</sub>Ag<sub>0.03</sub> NSA NP embedded in an epoxy resin. (B) Atomic resolution STEM-HAADF image of the C-Cu<sub>0.97</sub>Ag<sub>0.03</sub> NSA edge indicated with the (1) denotation in (A). (C-D) EDXS elemental maps of Cu (C) and Ag (D) in the region shown in (B). (E) EDX spectra of the core and edge regions of the C-Cu<sub>0.97</sub>Ag<sub>0.03</sub> NSA (indicated in B-D) showing the presence of the characteristic Ag L $\alpha$  and L $\beta$  EDXS peaks at edge regions only, corresponding to the first 6 MLs of the particle. (F) Line scan of intensity over the image in (B).

**Figure 5. Electrocatalysis of (an)isotropic Cu-Ag NPs and NSAs.** Error bars represent the mean ( $\mu$ ) + standard deviation (SD) of three independent measurements. Ball models in the title indicate the geometrical description of the anisotropic particles consisting of Cu(100) facets in orange, Cu(111) facets in yellow, edge sites in red and corner sites in red brown; and Ag is indicated in turquoise. (A) Product distribution of the C- Th- and TOh-Cu NCs. (B) Product distribution of the anisotropic Th-Cu<sub>0.97</sub>Ag<sub>0.03</sub>, C-Cu<sub>0.97</sub>Ag<sub>0.03</sub> and TOh-Cu<sub>0.97</sub>Ag<sub>0.03</sub> NSA. (C) C<sub>2+</sub> selectivity as a function of facet and composition. (D) C<sub>2+</sub> liquid fuel selectivity as a function of facet and composition. The interface between Cu-Ag(111) and Cu-Ag(100) offers evidently the best C<sub>2+</sub> liquid fuel producing active sites.

**Figure 6. Phase-segregation of Cu-Ag NSAs during CO<sub>2</sub>RR.** (A, D, G) Time evolution of the product distributions of the Th-Cu-Ag NSA (A), C-Cu-Ag NSA (D), and TOh-Cu-Ag NSA (G) at -1.1 V vs RHE in CO<sub>2</sub>-saturated 0.1 M KHCO<sub>3</sub>. C<sub>1</sub> products including HCOO<sup>-</sup>, CO and CH<sub>4</sub> are depicted in orange. C<sub>2+</sub> liquid fuels products including CH<sub>3</sub>COO<sup>-</sup>, CH<sub>3</sub>CHO, CH<sub>3</sub>CH<sub>2</sub>OH, C<sub>3</sub>H<sub>7</sub>OH are depicted in blue. C<sub>2</sub>H<sub>4</sub> is depicted in purple and H<sub>2</sub> in grey. Error bars indicate mean ( $\mu$ ) + standard deviation (SD) of three-independent measurements (**Table**



**S6).** Liquid products are collected under operation from a gas-tight H-cell using a clean syringe. (B, E, H) BF-TEM images of the pristine Th-Cu-Ag NSA (B), C-Cu-Ag NSA (E), and TOh-Cu-Ag-NSA (H). (C, F, I) Negative contrast BF-TEM images of the Th-Cu-Ag NSA (C), C-Cu-Ag NSA (F), and TOh-Cu-Ag-NSA (I) electrocatalyst after 30 min of CO<sub>2</sub>RR. Negative contrast images are offered as a visual-aid to observe the extrusions with higher contrast at the particle surfaces (indicated with arrows) assigned to the Ag phase. Note that the alternating bright/dark areas in the BF-TEM images are the result of thickness-fringes.

**Figure 7. Theory-guided optimization of the ternary alloy system.** (A) Activity-selectivity plot of CO<sub>2</sub>RR/CORR of the Cu-Ag-Pd ternary alloy system. Orange colored dots indicate compositions with  $\geq 74$  at.% Cu, light blue and purple colored with  $< 74$  at.% Cu and  $> 13$  at.% Ag and Pd, respectively. Black symbols (circle, star and square) denote the predicted values from the machine learning-based algorithm. Blue symbols and error bars indicate molar yields as calculated from experimental data in (C) and **Table S8** and **S9**. (B) STEM-EDXS elemental map of Cu (orange), Ag (turquoise), and Pd (purple) in as-synthesized C-Cu<sub>79</sub>Ag<sub>6</sub>Pd<sub>16</sub> NSA with Ag:Pd equals 1:3. (C) Time averaged FEs of C<sub>2</sub>+ liquid fuels, C<sub>2</sub>H<sub>4</sub> and H<sub>2</sub> of the C-Cu<sub>79</sub>Ag<sub>21</sub>, C-Cu<sub>79</sub>Ag<sub>16</sub>Pd<sub>5</sub> and C-Cu<sub>79</sub>Pd<sub>16</sub>Ag<sub>5</sub> NSAs, respectively. Electrochemical test was performed for 30 min at  $-1.1$  V vs. RHE in 0.1 M KHCO<sub>3</sub>. Square, circle and star insets reflect matching composition in (A)-(C). Error bars indicate the mean ( $\mu$ ) + standard deviation (SD) of three independent measurements.

### 13. References

- (1) Cui, C.; Gan, L.; Heggen, M.; Rudi, S.; Strasser, P. Compositional Segregation in Shaped Pt Alloy Nanoparticles and Their Structural Behaviour during Electrocatalysis. **Nat. Mater.** 2013, 12, 765–771.
- (2) Niu, Z.; Becknell, N.; Yu, Y.; Kim, D.; Chen, C.; Kornienko, N.; Somorjai, G. A.; Yang, P. Anisotropic Phase Segregation and Migration of Pt in Nanocrystals En Route to Nanoframe Catalysts. **Nat. Mater.** 2016, 15, 1188–1194.
- (3) Taccardi, N.; Grabau, M.; Debuschewitz, J.; Distaso, M.; Brandl, M.; Hock, R.; Maier, F.; Papp, C.; Erhard, J.; Neiss, C.; Peukert, W.; Görling, A.; Steinrück, H.-P.; Wasserscheid, P. Gallium-Rich Pd–Ga Phases as Supported Liquid Metal Catalysts. **Nat. Chem.** 2017, 9, 862–867.
- (4) Zhou, L.; Swearer, D. F.; Zhang, C.; Robotjazi, H.; Zhao, H.; Henderson, L.; Dong, L.; Christopher, P.; Carter, E. A.; Nordlander, P.; Halas, N. J. Quantifying Hot Carrier and Thermal Contributions in Plasmonic Photocatalysis. **Science** 2018, 362, 69–72.
- (5) Batchelor, T. A. A.; Pedersen, J. K.; Winther, S. H.; Castelli, I. E.; Jacobsen, K. W.; Rossmeisl, J. High-Entropy Alloys as a Discovery Platform for Electrocatalysis. **Joule** 2019, 3, 834–845.

- 542 (6) Zhang, X.; Han, S.; Zhu, B.; Zhang, G.; Li, X.; Gao, Y.; Wu, Z.; Yang, B.; Liu, Y.; Baaziz,  
543 W.; Ersen, O.; Gu, M.; Miller, J. T.; Liu, W. Reversible Loss of Core–Shell Structure for Ni–  
544 Au Bimetallic Nanoparticles during CO<sub>2</sub> Hydrogenation. **Nat. Catal.** 2020, 3, 411–417.
- 545 (7) Xing, F.; Nakaya, Y.; Yasumura, S.; Shimizu, K.; Furukawa, S. Ternary Platinum–Cobalt–  
546 Indium Nanoalloy on Ceria as a Highly Efficient Catalyst for the Oxidative Dehydrogenation  
547 of Propane Using CO<sub>2</sub>. **Nat. Catal.** 2022, 5, 55–65.
- 548 (8) Pedersen, J. K.; Batchelor, T. A. A.; Bagger, A.; Rossmeisl, J. High-Entropy Alloys as  
549 Catalysts for the CO<sub>2</sub> and CO Reduction Reactions. **ACS Catal.** 2020, 10, 2169–2176.
- 550 (9) Sankar, M.; Dimitratos, N.; Miedziak, P. J.; Wells, P. P.; Kiely, C. J.; Hutchings, G. J.  
551 Designing Bimetallic Catalysts for a Green and Sustainable Future. **Chem. Soc. Rev.** 2012, 41,  
552 8099–8139.
- 553 (10) Xie, C.; Niu, Z.; Kim, D.; Li, M.; Yang, P. Surface and Interface Control in Nanoparticle  
554 Catalysis. **Chem. Rev.** 2020, 120, 1184–1249.
- 555 (11) Tabrizi, N. S.; Xu, Q.; van der Pers, N. M.; Schmidt-Ott, A. Generation of Mixed Metallic  
556 Nanoparticles from Immiscible Metals by Spark Discharge. **J. Nanoparticle Res.** 2010, 12,  
557 247–259.
- 558 (12) Kane, K. A.; Reber, A. C.; Khanna, S. N.; Bertino, M. F. Laser Synthesized Nanoparticle  
559 Alloys of Metals with Bulk Miscibility Gaps. **Prog. Nat. Sci. Mater. Int.** 2018, 28, 456–463.
- 560 (13) Feng, J.; Ramlawi, N.; Biskos, G.; Schmidt-Ott, A. Internally Mixed Nanoparticles from  
561 Oscillatory Spark Ablation between Electrodes of Different Materials. **Aerosol Sci. Technol.**  
562 2018, 52, 505–514.
- 563 (14) Yao, Y.; Huang, Z.; Xie, P.; Lacey, S. D.; Jacob, R. J.; Xie, H.; Chen, F.; Nie, A.; Pu, T.;  
564 Rehwoldt, M.; Yu, D.; Zachariah, M. R.; Wang, C.; Shahbazian-Yassar, R.; Li, J.; Hu, L.  
565 Carbothermal Shock Synthesis of High-Entropy-Alloy Nanoparticles. **Science** 2018, 359,  
566 1489–1494.
- 567 (15) Yang, C.; Ko, B. H.; Hwang, S.; Liu, Z.; Yao, Y.; Luc, W.; Cui, M.; Malkani, A. S.; Li, T.;  
568 Wang, X.; Dai, J.; Xu, B.; Wang, G.; Su, D.; Jiao, F.; Hu, L. Overcoming Immiscibility toward  
569 Bimetallic Catalyst Library. **Sci. Adv.** 2020, 6, eaaz6844.
- 570 (16) Guntern, Y. T.; Okatenko, V.; Pankhurst, J.; Varandili, S. B.; Iyengar, P.; Koolen, C.; Stoian,  
571 D.; Vavra, J.; Buonsanti, R. Colloidal Nanocrystals as Electrocatalysts with Tunable Activity  
572 and Selectivity. **ACS Catal.** 2021, 11, 1248–1295.
- 573 (17) Hori, Y.; Takahashi, I.; Koga, O.; Hoshi, N. Selective Formation of C<sub>2</sub> Compounds from  
574 Electrochemical Reduction of CO<sub>2</sub> at a Series of Copper Single Crystal Electrodes. **J. Phys.**  
575 **Chem. B** 2002, 106, 15–17.
- 576 (18) Loiudice, A.; Lobaccaro, P.; Kamali, E. A.; Thao, T.; Huang, B. H.; Ager, J. W.; Buonsanti, R.  
577 Tailoring Copper Nanocrystals towards C<sub>2</sub> Products in Electrochemical CO<sub>2</sub> Reduction.  
578 **Angew. Chem. Int. Ed.** 2016, 55, 5789–5792.
- 579 (19) Iyengar, P.; Huang, J.; Gregorio, G. L. D.; Gadiyar, C.; Buonsanti, R. Size Dependent  
580 Selectivity of Cu Nano-Octahedra Catalysts for the Electrochemical Reduction of CO<sub>2</sub> to CH<sub>4</sub>.  
581 **Chem. Commun.** 2019, 55, 8796–8799.
- 582 (20) Schouten, K. J. P.; Pérez Gallent, E.; Koper, M. T. M. Structure Sensitivity of the  
583 Electrochemical Reduction of Carbon Monoxide on Copper Single Crystals. **ACS Catal.** 2013,  
584 3, 1292–1295.
- 585 (21) Clark, E. L.; Hahn, C.; Jaramillo, T. F.; Bell, A. T. Electrochemical CO<sub>2</sub> Reduction over  
586 Compressively Strained CuAg Surface Alloys with Enhanced Multi-Carbon Oxygenate  
587 Selectivity. **J. Am. Chem. Soc.** 2017, 139, 15848–15857.
- 588 (22) Higgins, D.; Landers, A. T.; Ji, Y.; Nitopi, S.; Morales-Guio, C. G.; Wang, L.; Chan, K.; Hahn,  
589 C.; Jaramillo, T. F. Guiding Electrochemical Carbon Dioxide Reduction toward Carbonyls  
590 Using Copper Silver Thin Films with Interphase Miscibility. **ACS Energy Lett.** 2018, 3,  
591 2947–2955.
- 592 (23) Wang, X.; Ou, P.; Ozden, A.; Hung, S.-F.; Tam, J.; Gabardo, C. M.; Howe, J. Y.; Sisler, J.;  
593 Bertens, K.; García de Arquer, F. P.; Miao, R. K.; O’Brien, C. P.; Wang, Z.; Abed, J.; Rasouli,  
594 A. S.; Sun, M.; Ip, A. H.; Sinton, D.; Sargent, E. H. Efficient Electrosynthesis of N-Propanol  
595 from Carbon Monoxide Using a Ag–Ru–Cu Catalyst. **Nat. Energy** 2022, 7, 170–176.

- 596 (24) Xia, X.; Wang, Y.; Ruditskiy, A.; Xia, Y. 25th Anniversary Article: Galvanic Replacement: A  
597 Simple and Versatile Route to Hollow Nanostructures with Tunable and Well-Controlled  
598 Properties. **Adv. Mater.** 2013, 25, 6313–6333.
- 599 (25) Subramanian, P. R.; Perepezko, J. H. The Ag-Cu (Silver-Copper) System. **J. Phase Equilibria**  
600 1993, 14, 62–75.
- 601 (26) Kim, N. R.; Shin, K.; Jung, I.; Shim, M.; Lee, H. M. Ag-Cu Bimetallic Nanoparticles with  
602 Enhanced Resistance to Oxidation: A Combined Experimental and Theoretical Study. **J. Phys.**  
603 **Chem. C** 2014, 118, 26324–26331.
- 604 (27) Lee, C.; Kim, N. R.; Koo, J.; Lee, Y. J.; Lee, H. M. Cu-Ag Core-Shell Nanoparticles with  
605 Enhanced Oxidation Stability for Printed Electronics. **Nanotechnology** 2015, 26, 455601.
- 606 (28) Osowiecki, W. T.; Ye, X.; Satish, P.; Bustillo, K. C.; Clark, E. L.; Alivisatos, A. P. Tailoring  
607 Morphology of Cu-Ag Nanocrescents and Core-Shell Nanocrystals Guided by a  
608 Thermodynamic Model. **J. Am. Chem. Soc.** 2018, 140, 8569–8577.
- 609 (29) Huang, J.; Mensi, M.; Oveisi, E.; Mantella, V.; Buonsanti, R. Structural Sensitivities in  
610 Bimetallic Catalysts for Electrochemical CO<sub>2</sub> Reduction Revealed by Ag-Cu Nanodimers. **J.**  
611 **Am. Chem. Soc.** 2019, 141, 2490–2499.
- 612 (30) Hoang, T. T. H.; Verma, S.; Ma, S.; Fister, T. T.; Timoshenko, J.; Frenkel, A. I.; Kenis, P. J.  
613 A.; Gewirth, A. A. Nanoporous Copper-Silver Alloys by Additive-Controlled  
614 Electrodeposition for the Selective Electroreduction of CO<sub>2</sub> to Ethylene and Ethanol. **J. Am.**  
615 **Chem. Soc.** 2018, 140, 5791–5797.
- 616 (31) Dettelbach, K. E.; He, J.; Johnson, N. J. J.; Huang, A.; Bottomley, A.; Lam, B.; Salvatore, D.  
617 A.; Berlinguette, C. P. Kinetic Phases of Ag-Cu Alloy Films Are Accessible through  
618 Photodeposition. **J. Mater. Chem. A** 2019, 7, 711–715.
- 619 (32) Ruban, A. V.; Skriver, H. L.; Nørskov, J. K. Surface Segregation Energies in Transition-Metal  
620 Alloys. **Phys. Rev. B** 1999, 59, 15990–16000.
- 621 (33) Koolen, C. D.; Torrent, L.; Agarwal, A.; Meili-Borovinskaya, O.; Gasilova, N.; Li, M.; Luo,  
622 W.; Züttel, A. High-Throughput Sizing, Counting, and Elemental Analysis of Anisotropic  
623 Multimetallic Nanoparticles with Single-Particle Inductively Coupled Plasma Mass  
624 Spectrometry. **ACS Nano** 2022.
- 625 (34) Tran, R.; Xu, Z.; Radhakrishnan, B.; Winston, D.; Sun, W.; Persson, K. A.; Ong, S. P. Surface  
626 Energies of Elemental Crystals. **Sci. Data** 2016, 3, 160080.
- 627 (35) Koolen, C. D.; Luo, W.; Züttel, A. From Single Crystal to Single Atom Catalysts: Structural  
628 Factors Influencing the Performance of Metal Catalysts for CO<sub>2</sub> Electroreduction. **ACS Catal.**  
629 2022, 948–973.
- 630 (36) Sprunger, P. T.; Lægsgaard, E.; Besenbacher, F. Growth of Ag on Cu(100) Studied by STM:  
631 From Surface Alloying to Ag Superstructures. **Phys. Rev. B** 1996, 54, 8163–8171.
- 632 (37) *Many-Particle Spectroscopy of Atoms, Molecules, Clusters, and Surfaces*; Berakdar, J.,  
633 Kirschner, J., Eds.; Springer US, 2001.
- 634 (38) Kim, D.; Resasco, J.; Yu, Y.; Asiri, A. M.; Yang, P. Synergistic Geometric and Electronic  
635 Effects for Electrochemical Reduction of Carbon Dioxide Using Gold-Copper Bimetallic  
636 Nanoparticles. **Nat. Commun.** 2014, 5, 1–8.
- 637 (39) Frenkel, A. I.; Yevick, A.; Cooper, C.; Vasic, R. Modeling the Structure and Composition of  
638 Nanoparticles by Extended X-Ray Absorption Fine-Structure Spectroscopy. **Annu. Rev. Anal.**  
639 **Chem.** 2011, 4, 23–39.
- 640 (40) Sun, D. T.; Peng, L.; Reeder, W. S.; Moosavi, S. M.; Tiana, D.; Britt, D. K.; Oveisi, E.; Queen,  
641 W. L. Rapid, Selective Heavy Metal Removal from Water by a Metal-Organic  
642 Framework/Polydopamine Composite. **ACS Cent. Sci.** 2018, 4, 349–356.
- 643 (41) Bencan, A.; Oveisi, E.; Hashemizadeh, S.; Veerapandiyan, V. K.; Hoshina, T.; Rojac, T.;  
644 Deluca, M.; Drazic, G.; Damjanovic, D. Atomic Scale Symmetry and Polar Nanoclusters in the  
645 Paraelectric Phase of Ferroelectric Materials. **Nat. Commun.** 2021, 12, 3509.
- 646 (42) Anderko, M. H. and K. *Constitution of Binary Alloys, SECOND EDITION*, Second Edition.;  
647 McGraw Hill Book Company: New York, NY, 1958.
- 648 (43) Tsaur, B. Y.; Lau, S. S.; Mayer, J. W. Continuous Series of Metastable Ag-Cu Solid Solutions  
649 Formed by Ion-beam Mixing. **Appl. Phys. Lett.** 1980, 36, 823–826.

- (44) Cheng, H.; Wang, C.; Qin, D.; Xia, Y. Galvanic Replacement Synthesis of Metal Nanostructures: Bridging the Gap between Chemical and Electrochemical Approaches. **Acc. Chem. Res.** 2023, 56, 900–909.
- (45) Bratsch, S. G. Standard Electrode Potentials and Temperature Coefficients in Water at 298.15 K. **J. Phys. Chem. Ref. Data** 1989, 18, 1–21.
- (46) Hori, Y.; Takahashi, I.; Koga, O.; Hoshi, N. Selective Formation of C<sub>2</sub> Compounds from Electrochemical Reduction of CO<sub>2</sub> at a Series of Copper Single Crystal Electrodes. **J. Phys. Chem. B** 2002, 106, 15–17.
- (47) Hori, Y.; Takahashi, I.; Koga, O.; Hoshi, N. Electrochemical Reduction of Carbon Dioxide at Various Series of Copper Single Crystal Electrodes. **J. Mol. Catal. Chem.** 2003, 199, 39–47.
- (48) Wu, Z.-Z.; Zhang, X.-L.; Niu, Z.-Z.; Gao, F.-Y.; Yang, P.-P.; Chi, L.-P.; Shi, L.; Wei, W.-S.; Liu, R.; Chen, Z.; Hu, S.; Zheng, X.; Gao, M.-R. Identification of Cu(100)/Cu(111) Interfaces as Superior Active Sites for CO Dimerization During CO<sub>2</sub> Electroreduction. **J. Am. Chem. Soc.** 2022, 144, 259–269.
- (49) Salehi-Khojin, A.; Jhong, H.-R. M.; Rosen, B. A.; Zhu, W.; Ma, S.; Kenis, P. J. A.; Masel, R. I. Nanoparticle Silver Catalysts That Show Enhanced Activity for Carbon Dioxide Electrolysis. **J. Phys. Chem. C** 2013, 117, 1627–1632.
- (50) Wang, L.; Higgins, D. C.; Ji, Y.; Morales-Guio, C. G.; Chan, K.; Hahn, C.; Jaramillo, T. F. Selective Reduction of CO to Acetaldehyde with CuAg Electrocatalysts. **Proc. Natl. Acad. Sci.** 2020, 117, 12572–12575.
- (51) Progress and Perspectives of Electrochemical CO<sub>2</sub> Reduction on Copper in Aqueous Electrolyte | Chemical Reviews <https://pubs.acs.org/doi/10.1021/acs.chemrev.8b00705> (accessed 2020 -02 -29).
- (52) Iyengar, P.; Kolb, M. J.; Pankhurst, J. R.; Calle-Vallejo, F.; Buonsanti, R. Elucidating the Facet-Dependent Selectivity for CO<sub>2</sub> Electroreduction to Ethanol of Cu–Ag Tandem Catalysts. **ACS Catal.** 2021, 11, 4456–4463.
- (53) Iyengar, P.; Kolb, M. J.; Pankhurst, J.; Calle-Vallejo, F.; Buonsanti, R. Theory-Guided Enhancement of CO<sub>2</sub> Reduction to Ethanol on Ag–Cu Tandem Catalysts via Particle-Size Effects. **ACS Catal.** 2021, 11, 13330–13336.
- (54) Yu, J.; Wang, J.; Ma, Y.; Zhou, J.; Wang, Y.; Lu, P.; Yin, J.; Ye, R.; Zhu, Z.; Fan, Z. Recent Progresses in Electrochemical Carbon Dioxide Reduction on Copper-Based Catalysts toward Multicarbon Products. **Adv. Funct. Mater.** 2021, 31, 2102151.
- (55) Nørskov, J. K.; Bligaard, T.; Rossmeisl, J.; Christensen, C. H. Towards the Computational Design of Solid Catalysts. **Nat. Chem.** 2009, 1, 37–46.
- (56) Zhou, Y.; Che, F.; Liu, M.; Zou, C.; Liang, Z.; De Luna, P.; Yuan, H.; Li, J.; Wang, Z.; Xie, H.; Li, H.; Chen, P.; Bladt, E.; Quintero-Bermudez, R.; Sham, T.-K.; Bals, S.; Hofkens, J.; Sinton, D.; Chen, G.; Sargent, E. H. Dopant-Induced Electron Localization Drives CO<sub>2</sub> Reduction to C<sub>2</sub> Hydrocarbons. **Nat. Chem.** 2018, 10, 974–980.
- (57) Lum, Y.; Ager, J. W. Sequential Catalysis Controls Selectivity in Electrochemical CO<sub>2</sub> Reduction on Cu. **Energy Environ. Sci.** 2018, 11, 2935–2944.
- (58) Subramanian, P. R.; Laughlin, D. E. Cu-Pd (Copper-Palladium). **J. Phase Equilibria** 1991, 12, 231–243.
- (59) Bagger, A.; Ju, W.; Varela, A. S.; Strasser, P.; Rossmeisl, J. Electrochemical CO<sub>2</sub> Reduction: A Classification Problem. **ChemPhysChem** 2017, 18, 3266–3273.
- (60) Clausen, C. M.; Pedersen, J. K.; Batchelor, T. A. A.; Rossmeisl, J. Lattice Distortion Releasing Local Surface Strain on High-Entropy Alloys. **Nano Res.** 2022, 15, 4775–4779.
- (61) Mortensen, J. J.; Hansen, L. B.; Jacobsen, K. W. Real-Space Grid Implementation of the Projector Augmented Wave Method. **Phys. Rev. B** 2005, 71, 035109.
- (62) Enkovaara, J.; Rostgaard, C.; Mortensen, J. J.; Chen, J.; Dułak, M.; Ferrighi, L.; Gavnholt, J.; Glinzvad, C.; Haikola, V.; Hansen, H. A.; Kristoffersen, H. H.; Kuisma, M.; Larsen, A. H.; Lehtovaara, L.; Ljungberg, M.; Lopez-Acevedo, O.; Moses, P. G.; Ojanen, J.; Olsen, T.; Petzold, V.; Romero, N. A.; Stausholm-Møller, J.; Strange, M.; Tritsarlis, G. A.; Vanin, M.; Walter, M.; Hammer, B.; Häkkinen, H.; Madsen, G. K. H.; Nieminen, R. M.; Nørskov, J. K.; Puska, M.; Rantala, T. T.; Schiøtz, J.; Thygesen, K. S.; Jacobsen, K. W. Electronic Structure

704 Calculations with GPAW: A Real-Space Implementation of the Projector Augmented-Wave  
 705 Method. **J. Phys. Condens. Matter** 2010, 22, 253202.  
 706 (63) Larsen, A. H.; Mortensen, J. J.; Blomqvist, J.; Castelli, I. E.; Christensen, R.; Dułak, M.; Friis,  
 707 J.; Groves, M. N.; Hammer, B.; Hargus, C.; Hermes, E. D.; Jennings, P. C.; Jensen, P. B.;  
 708 Kermode, J.; Kitchin, J. R.; Kolsbjerg, E. L.; Kubal, J.; Kaasbjerg, K.; Lysgaard, S.;  
 709 Maronsson, J. B.; Maxson, T.; Olsen, T.; Pastewka, L.; Peterson, A.; Rostgaard, C.; Schiøtz, J.;  
 710 Schütt, O.; Strange, M.; Thygesen, K. S.; Vegge, T.; Vilhelmsen, L.; Walter, M.; Zeng, Z.;  
 711 Jacobsen, K. W. The Atomic Simulation Environment—a Python Library for Working with  
 712 Atoms. **J. Phys. Condens. Matter** 2017, 29, 273002.  
 713 (64) Hammer, B.; Hansen, L. B.; Nørskov, J. K. Improved Adsorption Energetics within Density-  
 714 Functional Theory Using Revised Perdew-Burke-Ernzerhof Functionals. **Phys. Rev. B** 1999,  
 715 59, 7413–7421.  
 716

